AGU PUBLICATIONS

JGR

Journal of Geophysical Research: Solid Earth

RESEARCH ARTICLE
10.1002/2017JB015288

Key Points:
- We find no evidence for active detachment faulting at the Rainbow oceanic core complex
- The ultramafic massif generates high levels of shallow, low-magnitude seismicity
- Serpentinization is a plausible mechanism for much of the observed seismicity

Supporting Information:
- Supporting Information S1

Correspondence to:
R. A. Sohn,
rsohn@whoi.edu

Citation:
Horning, G., Sohn, R. A., Canales, J. P., & Dunn, R. A. (2018). Local seismicity of the Rainbow massif on the Mid-Atlantic Ridge. *Journal of Geophysical Research: Solid Earth*, *123*, 1615–1630. https://doi.org/10.1002/2017JB015288

Received 4 DEC 2017
Accepted 16 JAN 2018
Accepted article online 20 JAN 2018
Published online 17 FEB 2018

Local Seismicity of the Rainbow Massif on the Mid-Atlantic Ridge

G. Horning[1], R. A. Sohn[2], J. P. Canales[2], and R. A. Dunn[3]

[1]Massachusetts Institute of Technology/Woods Hole Oceanographic Institution Joint Program in Oceanography/Applied Ocean Science and Engineering, Woods Hole, MA, USA, [2]Department of Geology and Geophysics, Woods Hole Oceanographic Institution, Woods Hole, MA, USA, [3]Department of Geology and Geophysics, School of Ocean and Earth Science and Technology, University of Hawai'i at Mānoa, Honolulu, HI, USA

Abstract The Rainbow massif, an oceanic core complex located in a nontransform discontinuity on the Mid-Atlantic Ridge (36°N), is notable for hosting high-temperature hydrothermal discharge through ultramafic rocks. Here we report results from a 9 month microearthquake survey conducted with a network of 13 ocean bottom seismometers deployed on and around the Rainbow massif as part of the MARINER experiment in 2013–2014. High rates (~300 per day) of low-magnitude (average M_L ~ 0.5) microearthquakes were detected beneath the massif. The hypocenters do not cluster along deeply penetrating fault surfaces and do not exhibit mainshock/aftershock sequences, supporting the hypothesis that the faulting associated with the exhumation of the massif is currently inactive. Instead, the hypocenters demarcate a diffuse zone of continuous, low-magnitude deformation at relatively shallow (< ~3 km) depths beneath the massif, sandwiched in between the seafloor and seismic reflectors interpreted to be magmatic sills driving hydrothermal convection. Most of the seismicity is located in regions where seismic refraction data indicate serpentinized ultramafic host rock, and although the seismic network we deployed was not capable of constraining the focal mechanism of most events, our analysis suggests that serpentinization may play an important role in microearthquake generation at the Rainbow massif.

1. Introduction

The Rainbow massif, located in a nontransform discontinuity (NTD) on the Mid-Atlantic Ridge (MAR, 36°N), is notable for hosting high-temperature (365°C) hydrothermal discharge through ultramafic rocks (Douville et al., 2002). While exposures of mantle rocks are common at slow-to-ultraslow mid-ocean ridges (MORs) like the MAR, particularly along sections with reduced magma supply (e.g., Cannat, 1993; Cannat et al., 1995), high-temperature hydrothermal discharge is more prevalently associated with volcanically accreted, rather than tectonically exhumed, terrains (Kelley & Shank, 2013). Theoretical arguments indicate that high-temperature hydrothermal discharge at MORs requires an underlying melt body (Cann & Strens, 1982; Thurnherr & Richards, 2001), but the nearest known neovolcanic activity to the Rainbow hydrothermal field (RHF) is located 15–20 km away on the Alvin Mid-Atlantic Ridge (AMAR) segment (German & Parson, 1998), and models for NTD formation typically invoke tectonic processes in an amagmatic environment (e.g., Gràcia et al., 2000; Grindlay & Fox, 1993; Spencer et al., 1997). These seemingly contradictory observations and models raise important questions about how the Rainbow massif was formed and the tectonic and magmatic processes that allow it to generate and sustain high-temperature hydrothermal fluid discharge.

The MARINER experiment (Canales et al., 2013) utilized shipboard geophysical surveys (Eason et al., 2016; Paulatto et al., 2015), active-source seismic refraction and reflection (Canales et al., 2017; Dunn et al., 2017) surveys, and a passive microearthquake survey to examine these issues. Here we report results from the microearthquake survey conducted with a network of ocean bottom seismometers (OBSs). We detected high rates of small microearthquakes beneath the massif that allow us to constrain the seismogenic processes presently deforming the ultramafic massif and examine the possible role of serpentinization in these processes. By interpreting our results along with those from the shipboard geophysical surveys, the active-source seismic surveys, and the extant geological data from the Rainbow site, we can also constrain the geological processes that formed the ultramafic massif and generate high-temperature hydrothermal convection.

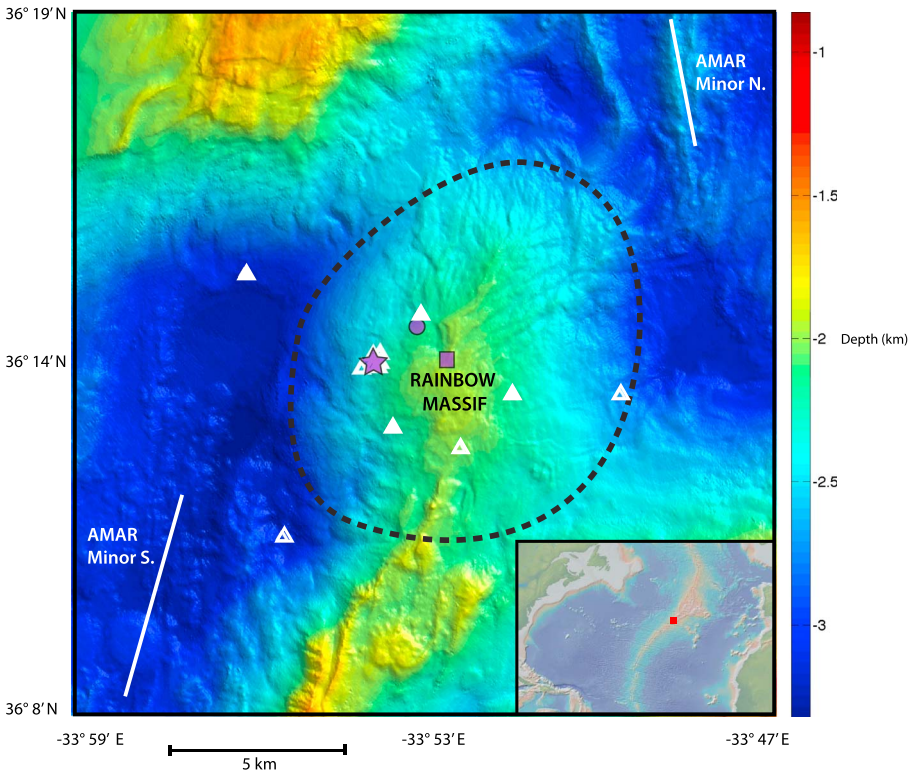

Figure 1. Bathymetry map of the Rainbow NTD (Paulatto et al., 2015). The Rainbow massif (demarcated with dashed black line) is located between the AMAR Minor N and AMAR Minor S spreading segments (indicated with white lines). The purple star marks the location of active hydrothermal venting, and the purple circle and square show fossil venting sites Ghost City and Clamstone, respectively. The white triangles show the location of the 13 OBSs that provided data for our analyses. Note that six OBS are clustered in a tight configuration around the active vent field. Inset shows location of the study area along the MAR.

2. Geological Setting

The Rainbow massif (Figure 1) is located in a small NTD of the MAR surrounded by en échelon nodal basins (Gràcia et al., 2000; Parson et al., 2000) that offset the AMAR and AMAR minor segments of the ridge by 19.6 km in distance and 1.1 Myr in age (German, Parson, & Team, 1996). Rainbow is one of a sequence of 10 NTDs found south of the Azores, many of which host active or fossil hydrothermal systems (Gràcia et al., 2000). Based on morphological and lithological observations, Andreani et al. (2014) argue that the dome-shaped massif is an oceanic core complex (OCC) uplifted along a west dipping detachment fault that is currently inactive. They find that the oblique orientation of fault traces crosscutting the massif and the focal mechanism (Dziewonski et al., 1981; Ekstrom et al., 2012) of a teleseismic event just south of the massif both indicate a ~30° clockwise rotation of the axis of least compressive stress with respect to the spreading direction. In 2005–2007 the Mid-Atlantic Ridge Comprehensive Hydrophone Experiment (MARCHE) autonomous hydrophone array (Simao et al., 2010) recorded scattered seismic activity in this region but did not delineate any obvious tectonic features. Paulatto et al. (2015) estimate that tectonic strain accommodates 60–80% of crustal accretion at the Rainbow NTD. Using bathymetry, gravity and magnetics, Paulatto et al. (2015) document the presence of at least two other OCCs on the fossil trace of the NTD, suggesting that exhumation of mantle rocks by detachment faulting has been a common process within the NTD during at least the last ~3.5 Myr.

The Rainbow massif is largely covered by pelagic sediments with minor amounts of carbonates (Andreani et al., 2014; Eason et al., 2016). Where basement is exposed, dredges and submersible observations document that highly serpentinized mantle is the most abundant rock type (Andreani et al., 2014). Ultramafics show varied textures representing a history of plastic deformation, hydrothermal alteration, static and syntectonic serpentinization, and intrusions of mafic material showing greenschist facies alteration (talc-tremolite-chlorite) (Andreani et al., 2014). Exposures of mafic plutonic rocks are rare (recovered in only 6 of the 29 dredges reported in Andreani et al., 2014) and are consistently associated with serpentinized peridotites throughout the core of the massif (Andreani et al., 2014). Most of these rocks are undeformed, although

some present evidence for plastic deformation or ductile-to-brittle deformation bands (Andreani et al., 2014). Exposures of volcanic rocks are also rare and outcrop preferentially on the northern and southern edges of the massif (Andreani et al., 2014).

High-temperature hydrothermal venting on the massif presently occurs through 10 active black smoker chimneys (Fouquet et al., 1998), forming the RHF (Figure 1). Two fossil low-temperature hydrothermal sites (Ghost City and Clamstone) have also been documented (Lartaud et al., 2010, 2011). Vent fluids from the RHF are high in H_2 and CH_4 compared to other MAR systems, indicating that serpentinization influences the vent fluid chemistry (Fouquet et al., 1998). Through a detailed investigation of the Rainbow plume, German et al. (2010) estimated volume and heat fluxes from the RHF of 450 L/s and 0.5 GW, respectively, whereas Thurnherr and Richards (2001) estimate a heat flow of 1–5 GW from the plume data. Active and fossil hydrothermal activity at Rainbow is associated with recent faults and fractures, suggesting that extensional faulting throughout the center of the massif localizes fluid discharge zones (Andreani et al., 2014).

3. Data Processing and Results

Fifteen OBSs were free-fall deployed on and around the Rainbow Massif (Figure 1) as part of the MARINER experiment aboard the R/V *Marcus G. Langseth* on cruise MGL1305 (Canales et al., 2013), but two of the instruments were not recovered due to failures in their anchor release systems The seismic network consisted of three rings of instruments centered on the massif, each with a different aperture: (1) four instruments (three recovered) were deployed on a 5 km radius ring, (2) five instruments (four recovered) were deployed on a 2 km radius ring, and (3) six instruments were deployed in a tight cluster around the active venting site ($<$500 m separation) (Figure 1). The deployment strategy allowed us to detect seismicity at scales ranging from tectonic activity associated with extension and deformation within the NTD to very small events associated with hydrothermal flow. Each instrument contained a short-period (4.5 Hz natural period), three-component geophone and a High Tech HTI-90-U hydrophone, with all channels recorded at 200 Hz. The instruments started recording in May 2013 and were recovered aboard the R/V *Pelagia* in January 2014, providing 9 months of continuous data. Data quality was generally good with comparable noise levels on all instruments (Figure 2), and high levels of seismic activity were recorded by all instruments.

The raw data were band-pass filtered at 8–20 Hz for event detection using the short-term average/long-term average (STA/LTA) algorithm available in the *Antelope* software package (www.brtt.com). A total of 80,135 locatable events were identified by associating arrivals on at least four stations during a 2 s window on the vertical channel, yielding a rate of ~300 events per day within a zone extending ~20 km along the ridge axis. The performance of the STA/LTA arrival time estimates was benchmarked against manual estimates for a subset of 300 randomly selected events. In many cases the arrival time estimates from the STA/LTA algorithm exhibited significant offsets from the manual arrival time picks, necessitating the use of a second automatic method to refine the picks. To accomplish this, we developed an algorithm that estimates phase arrival times based on the signal-to-noise ratio (SNR) of the earthquake signal in a 1 s sliding window. The details of this algorithm are described in the supporting information document.

Earthquake hypocenters were estimated using a grid search algorithm that calculated the weighted root mean square (rms) residual between the observed arrival times and those predicted by tracing rays through a 3-D velocity model derived from an active-source airgun refraction experiment (Dunn et al., 2017), with each arrival time pick weighted by the inverse of its uncertainty. *P* wave velocities in the 3-D model were defined on a 250 m grid spanning a 32 × 32 × 16 (*x*-*y*-*z*) km domain centered on the massif. A ray shooting algorithm (RAYTRACE3D; Menke, 2005) was used to estimate *P* wave travel times from each grid point in the velocity model to each instrument on the seafloor. *S* wave travel times were predicted by multiplying the *P* wave times by a constant factor (i.e., V_p/V_s ratio) of 2.05, chosen by systematically varying V_p/V_s from 1.5 to 2.1 and finding the value that minimized the rms residual for a subset of the 3,457 best recorded events (i.e., events detected by all stations and with the highest SNR arrivals). The best fitting V_p/V_s of 2.05 is a little higher than the range measured in MAR gabbroic rocks (1.76–1.94) (Miller & Christensen, 1997) but consistent with estimates for serpentinite (1.78–2.21) (Christensen, 2004). Hypocenter estimates were also made based on an average 1-D velocity model derived from the active-source refraction experiment, but the differences between the 1-D and 3-D results were small, and the results from the 3-D model are preferred as the hypocenters include the effect of the high-velocity ultramafic rocks underlying the massif on the event locations.

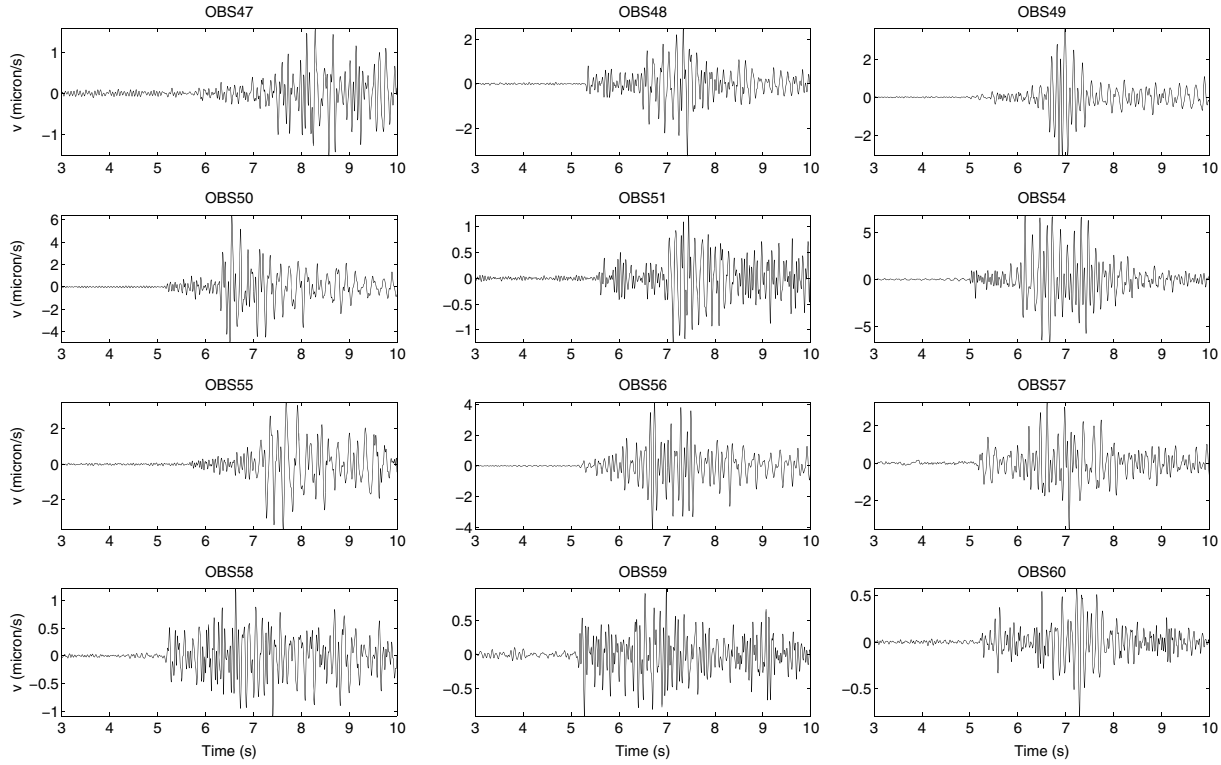

Figure 2. Waveform example (vertical component velocity) for a M_L 0.5 event recorded on all 13 instruments.

Hypocenter estimates (Sohn et al., 2018) correspond to the grid point that minimizes the rms residual for each event, and the final hypocenter estimates (Figures 3–5) were refined by applying a station correction to the *P* and *S* arrival times for each instrument to ensure that the mean rms for each station was ~0 s. For the entire deployment we were able to obtain hypocenter estimates for 80,135 events, and here we present hypocenters for the subset of 35,711 events that generated six or more phase arrivals across our network and had rms localization errors less than 200 ms. The mean value of the hypocentral uncertainties at the 1σ level are 0.78, 1.02, and 0.83 km in *x*, *y*, and *z*, respectively.

The hypocenters form a diffuse cloud within/beneath the ultramafic massif. To investigate whether this is a real feature or an artifact of the localization process, we conducted three tests. First, we assessed the sensitivity of the hypocentral pattern to location quality by plotting results using different rms error thresholds (see section S2 of the supporting information). These plots reveal no systematic differences in hypocentral patterns, indicating that the spread in the hypocenter locations is not due to poorly located events. Second, we attempted to use the relative relocation method *hypoDD* (Waldhauser & Ellsworth, 2000) to improve our hypocentral estimates. We applied the method to a subset of 1,000 well-recorded events but were not able to improve the hypocentral estimates using either the arrival time-based catalog method or the cross-correlation method. This is due to the fact that the individual microearthquake waveforms were not highly correlated (nearly all cross-correlation coefficients were <0.7) and that the grid search algorithm did not produce systematic errors that could be corrected based on relative arrival times. Third, we applied the collapsing method of Jones and Stewart (1997) to relocate the events. The collapsing method is a purely statistical method that does not consider the event waveforms or phase arrival times but rather the aggregate set of hypocentral spatial uncertainties (defined in our analysis at the 95% confidence level). Functionally, the collapsing method seeks the simplest geometric structure capable of explaining the observed seismicity pattern given the individual hypocentral uncertainties. The collapsing method migrated many events onto a discrete depth horizon at ~2–3 km below the seafloor and produced a small cluster of events beneath the center of the massif, but it did not change the lateral spread of the hypocenters, and it did not produce features that could be interpreted as fault structures (Figures 3 and 4). The fact that the collapsing method migrated many events onto a discrete depth horizon means that, given the depth

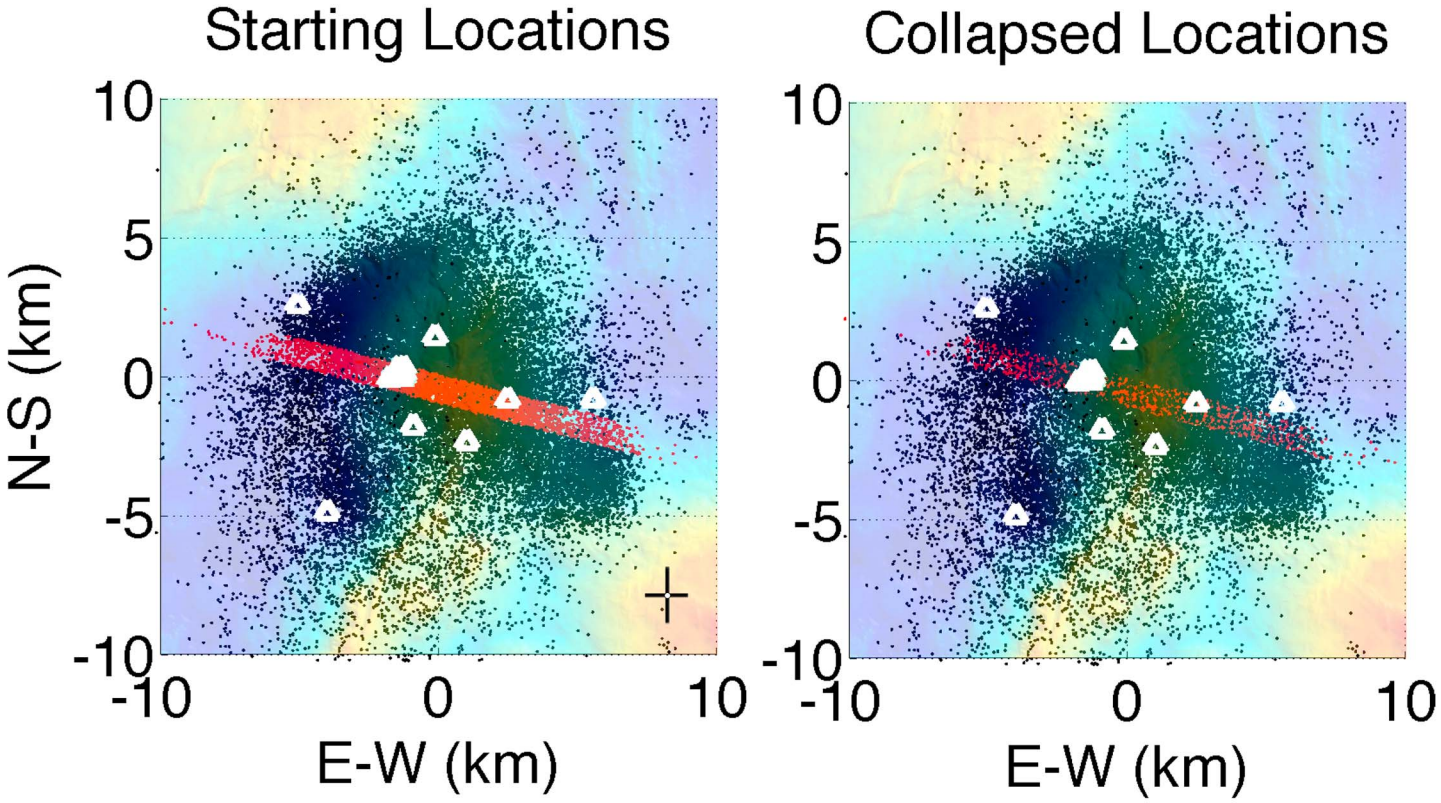

Figure 3. Microearthquake hypocenters with rms errors <200 ms and six or more phase picks across the network. The coordinate system for the axes is centered on the massif (−33.88792°W, 36.22967°N). (left) Epicenters from grid search method (black dots) shown on local bathymetry. OBS locations shown with white triangles. Average 1σ error bars for the catalog are shown in lower right corner. Events included in cross-section plots in Figure 4 are shown in red. (right) Epicenters after application of collapsing method. Symbols the same as in left panel.

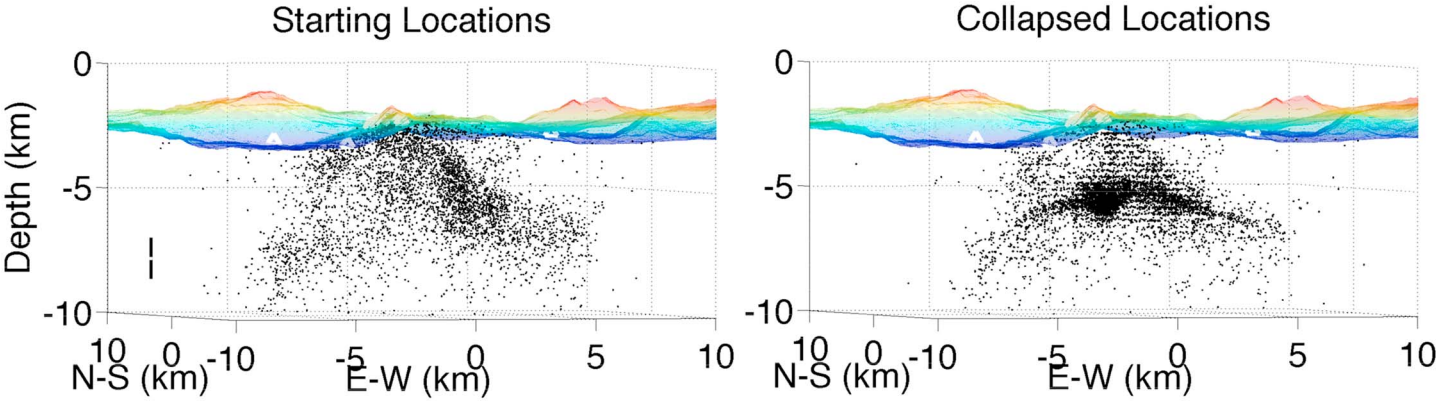

Figure 4. Perspective view of hypocenters along the cross section shown as a red band in Figure 3 (view is perpendicular to the cross section, looking from southwest corner of map to the northeast) with overlying bathymetry. The rest of the hypocenters in the catalog are stripped away to show how the depth of these events changes moving across the section. The north-south (N-S) and east-west (E-W) axes are labeled on the bottom of the grid. (left) Hypocenters from grid search method with average 1σ depth error bars for the catalog shown in bottom left corner. (right) Hypocenters after application of collapsing method.

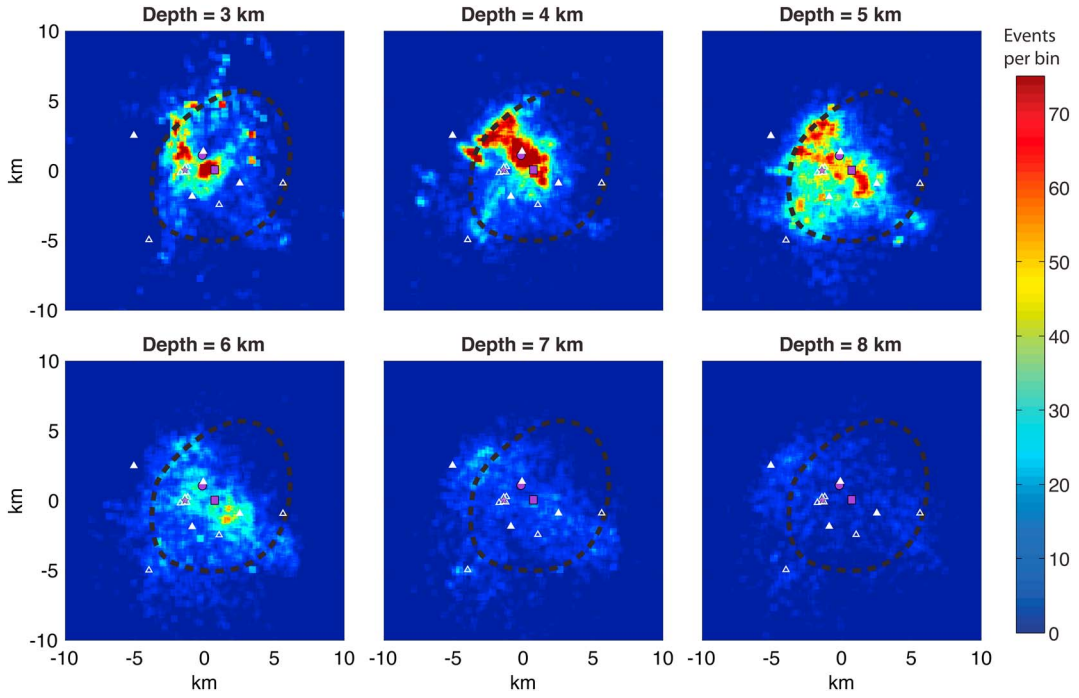

Figure 5. Density plot of hypocenter locations from the grid search method (i.e., "Starting Locations" in Figures 3 and 4) on a 500 m grid at different depths below sea level. On all panels the purple star marks the location of active hydrothermal venting and the purple square and circle mark the locations of fossil venting sites. The white triangles mark OBS locations. The dashed black line marks approximate surface exposure of the ultramafic massif.

uncertainties of the hypocentral estimates, many of the events could have been located on a discrete depth interval within the massif. By contrast, the fact that the overall lateral spread of the hypocenters was not changed by the collapsing method indicates that this aspect of the results is not due to lateral uncertainties in the localization process.

Based on the results of these tests, we conclude that the seismicity is indeed distributed across the entire lateral spread of the massif and that this aspect of our results is not an artifact of the data processing methods. The implications of the hypocenter patterns for seismogenesis at the massif are discussed in section 4 below. Our hypocenter analyses that follow are based on the absolute (as opposed to collapsed) catalog unless noted otherwise.

Earthquake moments were estimated based on the spectral levels of each event in the 4–20 Hz frequency band with corrections for propagation distance and radiation pattern (Brune, 1970; Hanks & Thatcher, 1972), and local magnitudes were estimated from the moments as described in Lee and Stewart (1981). Details of the moment and magnitude estimation procedure are provided in the supporting information, section S3. The average local magnitude of all events is ~0.5 with most events falling between −0.1 and 2 (Figure 6). The *b* value for the catalog of events is ~1.7 (Figure 7). Estimation of earthquake magnitude from local network data is subject to both systematic and random errors, and for small events these errors can be as large as a whole unit (Deichmann, 2006). While we cannot quantify the size of these errors for our data, they do not affect our *b* value estimate since essentially all of the seismicity is below the magnitude threshold of ~2–3 where the errors can cause a break in the cumulative magnitude plot (Deichmann, 2017). The small magnitudes of the microearthquakes and the high *b* value of the catalog indicate that absolute stress levels in the massif are relatively low (Scholz, 1968), with seismic moment release being accommodated by large numbers of small earthquakes. It is also possible that a significant fraction of moment release was accommodated by events that were too small to be detected by our network.

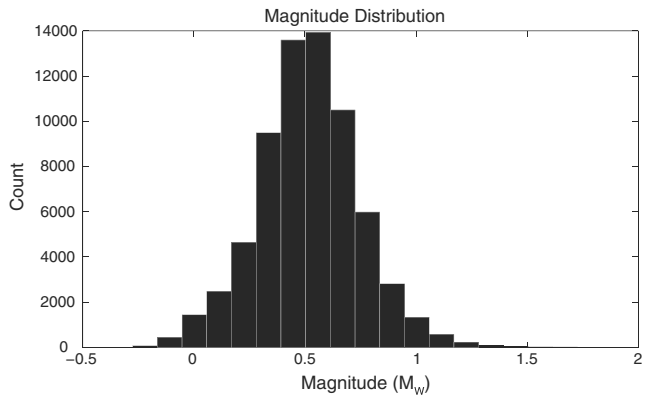

Figure 6. Histogram showing distribution of event local magnitudes.

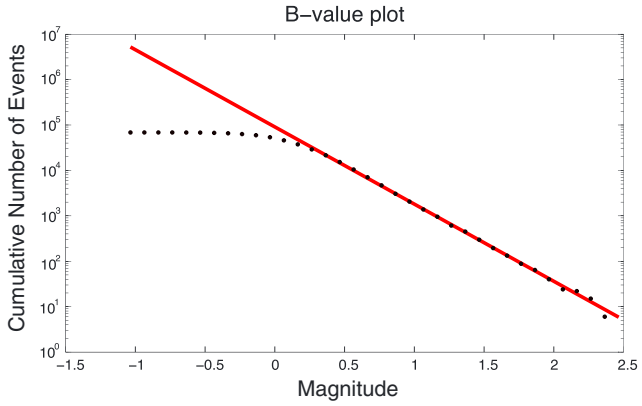

Figure 7. Open circles show cumulative number of events as a function of local magnitude. The red line indicates a *b* value of 1.7, which shows good fit to the data.

The seismicity rate is nearly linear throughout the 9 month deployment at a rate of ~300 events per day (Figure 8), with no indication of foreshock-aftershock sequences or swarms. There is no evidence for systematic space–time variations in the hypocentral data, with an essentially uniform rate of seismicity across the seismogenic zone for the entire deployment.

Focal mechanism estimates were attempted based on *P* wave first arrival polarities using the HASH software (Hardebeck & Shearer, 2002, 2003). However, given the relatively low number of instruments and the correspondingly high azimuthal gap for most events, the focal mechanism estimates using *P* wave polarities were generally not well constrained. We attempted to improve the focal mechanism constraints by including arrival amplitude information into the inversion for the 10 largest events in our catalog (i.e., best SNR). *S/V* and *S/H* wave amplitudes could be estimated for four stations because the orientation of their horizontal components could be constrained using direct water arrivals from airgun shots (the other stations were not recording during the active-source component of the MARINER experiment). Focal mechanism estimates incorporating arrival amplitudes were attempted using the method of Sileny et al. (2014) assuming both double-couple and shear-tensile crack source models. While most of the events still did not yield well-constrained estimates, a few provided evidence for oblique extension (Figure 9).

4. Discussion

The low-magnitude, high-rate seismicity that we observed at shallow depths beneath the Rainbow massif is markedly different from the results of previous microearthquake surveys at OCCs and has implications for the present-day state of tectonic and hydrothermal processes at the Rainbow site. We begin by relating our seismicity observations to previous work constraining the tectonics of the Rainbow NTD. We then compare the seismicity to observations from other OCCs on the MAR, which emphasizes the unique nature of our results. We conclude by assessing the plausibility of tectonic, thermal, and hydrothermal alteration (serpentinization) source mechanisms for the microearthquakes we observed.

4.1. Tectonics of the Rainbow NTD

Our microearthquake catalog contains a total moment release of 3×10^{14} N m over a period of 9 months, equivalent to a single $M_W = 3.6$ event. The seismicity occurred at a roughly constant rate of ~300 events per day (Figure 8) with a notable lack of mainshock/aftershock sequences or swarming activity. These results demonstrate that the massif was deformed by a high and essentially constant rate of low-magnitude, shallow seismicity during our deployment, with the majority of events occurring at depths less than 4 km depth below the seafloor and extending to the shallowest resolvable depths (250 m below seafloor) (Figures 4 and 5).

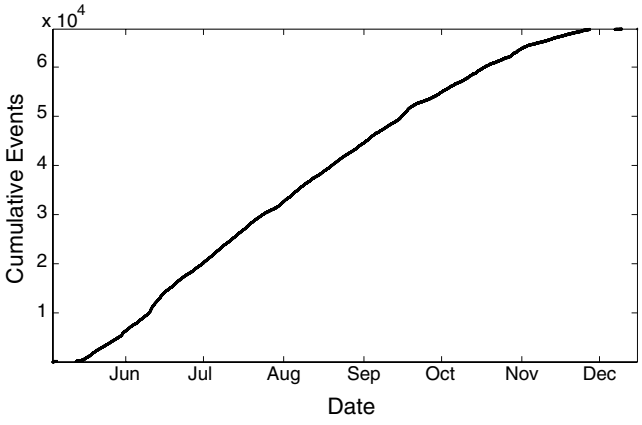

Figure 8. Seismicity rate during the experiment. The cumulative number of events is plotted versus time (month of year, 2013), revealing an essentially constant seismicity rate of ~300 per day.

Whereas previous microearthquake surveys of active oceanic detachment faults and OCCs have identified distinct faulting and deformation structures that penetrate into the mantle, often at a high (~70°) dip (Collins et al., 2012; deMartin et al., 2007; Grevemeyer et al., 2013; Parnell-Turner et al., 2017), the lack of any such features in our data suggests that if the Rainbow massif was exhumed along a detachment fault, such fault is no longer active. This supports the interpretation of (Andreani et al., 2014), based on the observation of a continuous and undisrupted sediment cover between the western flank of the massif and the nodal basin, that the Rainbow massif is no longer being exhumed. This interpretation is also consistent with shipboard geophysical data from the MARINER experiment, which indicates that the ridge offset that formed the Rainbow NTD is

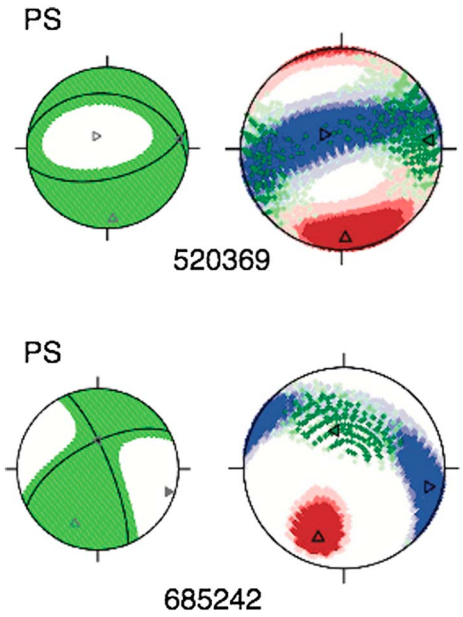

Figure 9. Focal mechanisms for two of the best constrained solutions from our event catalog. Estimates were derived using the method of Sileny et al. (2014) with *P* wave polarities from all stations and *P* and *S* wave amplitudes from four stations for which the sensor orientation could be constrained. (left column) The best fitting solution. (right column) The uncertainty of the pole location estimates on the focal sphere (blue = maximum compressive stress, green = intermediate compressive stress, red = minimum compressive stress).

migrating to the north into the AMAR Minor N segment where a new detachment fault is possibly forming, having accumulated 1 km of offset (Paulatto et al., 2015). This possible nascent detachment fault is located beyond the range of our OBS network, and so we are unable to determine if it is seismically active. Our interpretation that the Rainbow massif is no longer being exhumed must be caveated by the fact that our observation period (9 months) was short relative to tectonic and magmatic cycles at MORs, so we cannot formally rule out the possibility that large-scale faults associated with exhumation of the massif remain active but were dormant during our experiment.

The Rainbow massif is transected at an oblique angle by a set of roughly parallel faults, which have been interpreted to indicate that the massif itself is presently being extended rather than exhumed (Andreani et al., 2014; Eason et al., 2016). While the microearthquake hypocenters do not form discrete structures corresponding to these faults, many events occur at shallow depths directly beneath the seafloor expression of the faults, and oblique extension on shallow faults is broadly consistent with the focal mechanism results. We consider this hypothesis in more detail in section 4.3 below.

At very shallow depths ($<$ 1 km) below the seafloor there is a set of events on the northwest flank of the massif with hypocenters that are located (within error) along a shallow-dipping (15–30°) reflector observed in depth-migrated seismic reflection images (Figures 10b and 10c). The reflector intersects the seafloor just below the massif summit and extends ~3 km laterally to the slope break, reaching a depth of 1–1.5 km below the seafloor, delineating a ~3 km^2 terrain patch on the massif's northwest flank (Figure 10 inset). The seismicity data indicate that this reflector is associated with an actively slipping surface, and the size and shape of this surface are consistent with mass wasting on the flank of the ultramafic massif. Cannat et al. (2013) have described mass wasting features on the flanks of other ultramafic outcrops, and their observations suggest that flank failure in these settings occurs on low-angle slip planes via sliding of large, coherent blocks of ultramafic material. The seismicity and multichannel seismics (MCS) data from the northwest flank of the Rainbow massif are consistent with this scenario, suggesting that this form of mass wasting is presently ongoing at the site.

4.2. Seismicity Compared to Other OCCs

Several microearthquake studies have previously been conducted at OCCs on the MAR, providing a basis for comparison with our results. deMartin et al. (2007) observed an essentially constant seismicity rate (~80 events per day) during an 8 month OBS deployment at the Trans-Atlantic Geotraverse (TAG) segment of the MAR (26°N), but the earthquakes were on average 1–2 magnitude units larger than those we observed at Rainbow, and the hypocenters at TAG delineated an arcuate fault surface extending to depths $>$7 km below the seafloor, which was interpreted to represent a deeply penetrating, active oceanic detachment. In addition, almost no seismic activity was observed at depths shallower than ~3 km below the seafloor. These results contrast markedly with our seismicity patterns, which do not delineate any fault structures, and which are clustered at shallow depths beneath the Rainbow massif.

Atlantis massif (MAR, 30°N) is an inside-corner OCC bounded by a transform fault and consisting of a large gabbroic core surrounded by serpentinized peridotites (e.g., Blackman et al., 2011; Harding et al., 2016). Collins et al. (2012) found that seismicity at the Atlantis massif (~55 events per day) was concentrated in the axial valley rather than beneath the massif itself, which is located outboard of the axial valley on the inside corner of a ridge transform intersection. Some ridge-parallel normal-faulting events were observed beneath the massif, which were interpreted to represent flexural deformation of the exposed detachment surface, and asymmetry in the rift valley seismicity was interpreted to suggest that the detachment fault that formed the massif is possibly still active (Collins et al., 2012). More than half of the detected events were part of mainshock-aftershock sequences, although a ~100 day period of nearly constant rate seismicity was

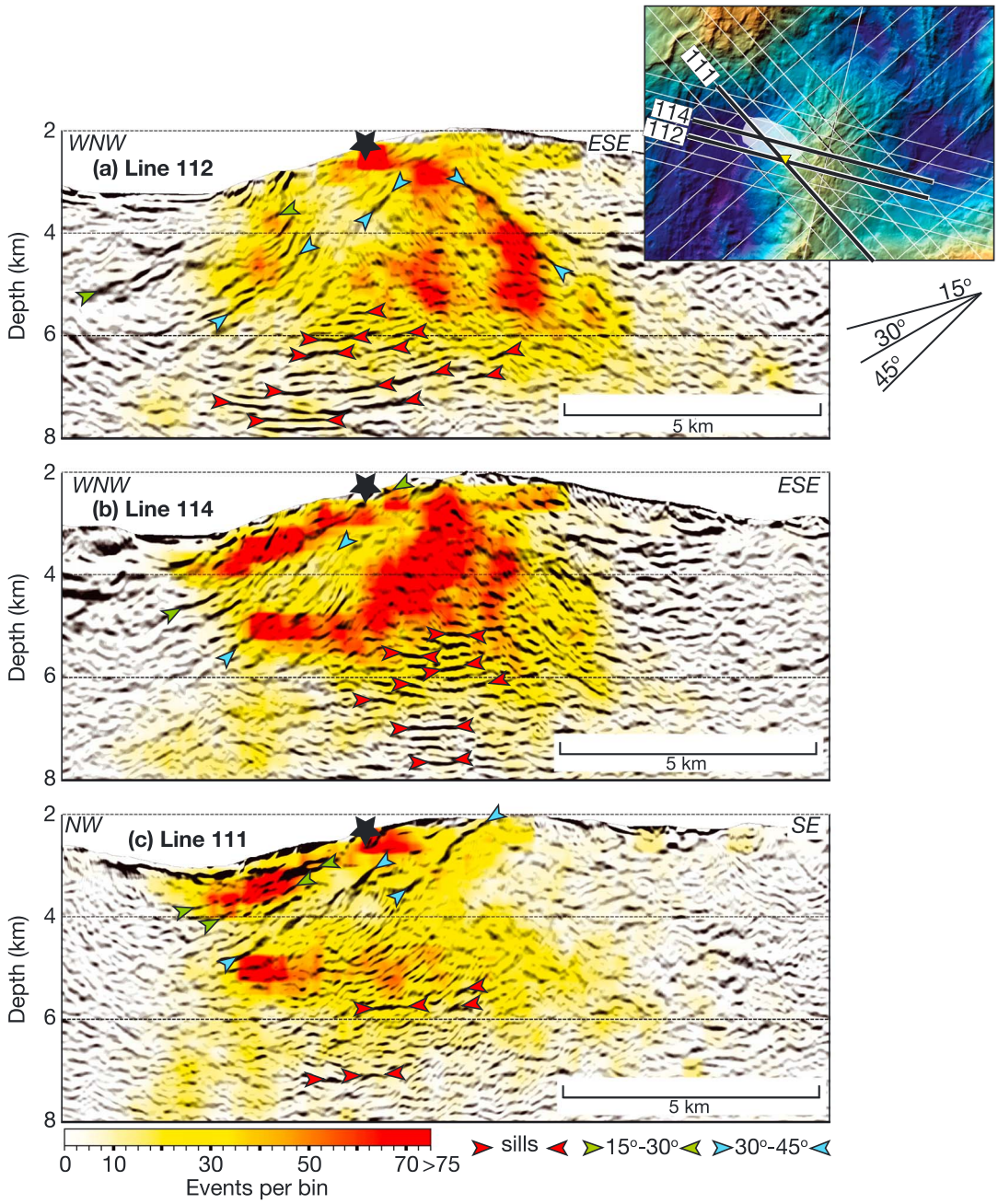

Figure 10. Multichannel seismic reflection images from Canales et al. (2017) plotted with microearthquake density. Green and blue arrowheads indicate dipping reflectors. Subhorizontal reflectors (red arrowheads) are interpreted as magmatic sills, most of which are thought to be solidified. Top right inset shows bathymetry and location of MCS reflection profiles, with the sections shown in this figure indicated in bold lines. Shaded region shows the areal extent of the shallow dipping reflector. Yellow triangle indicates location of active venting.

observed between two mainshock-aftershock sequences. The seismicity observed at the Atlantis massif thus contrasts markedly with our observations from the Rainbow massif in that the majority of activity occurred during mainshock-aftershock sequences associated with lithospheric extension in the axial valley and there was no activity at shallow depths beneath the massif.

Grevemeyer et al. (2013) report results from an OBS network deployed on the 15°N segment of the MAR, which includes the serpentine-hosted Logatchev hydrothermal field. Their results are more difficult to compare to ours because the station spacing of the seismic network (~5 km) was larger, which likely

precludes detection of small-magnitude events at shallow depths. Their network recorded an average of 24 locatable earthquakes per day, which were asymmetrically distributed on the east (versus west) side of the axial valley and interpreted to result from active detachment faulting at the Logatchev OCC. A small number of reverse faulting events were observed near the OCC, but the network lacked the hypocentral resolution required to determine the relationship of these events to the more ubiquitous normal faulting observed in the same area, and Grevemeyer et al. (2013) speculated that these reverse events may be associated with volume changes due to serpentinization or magma chamber filling. Regardless of the mechanism responsible for the reverse faulting, the seismicity observed at the Logatchev OCC is distinctly different from our observations at the Rainbow OCC. At Rainbow we observed an order of magnitude higher seismicity rate with a much higher proportion of small events relative to large events (Logatchev *b* value ~0.92 versus Rainbow *b* value ~1.7), and whereas seismicity at Rainbow is clustered at shallow depths directly beneath the massif, seismicity at Logatchev is deeper and distributed along the eastern side of the axial valley.

Most recently, Parnell-Turner et al. (2017) found two distinct bands of seismicity associated with active detachment faulting at the 13°20′N OCC on the MAR (~1,240 events per day, total). A deep band of normal faulting seismicity extends into the mantle on an arcuate fault surface, similar to the findings of deMartin et al. (2007) at the TAG OCC, while a second, shallower band of seismicity exhibits compressional focal mechanisms interpreted to represent the flexural response of the fault footwall to rollover and dome formation. These results provide insight into the mechanics of deformation on an active oceanic detachment fault, but, even though the relatively dense seismic network had small enough interelement spacings to detect shallow seismicity, low-magnitude events of the type we observed at the Rainbow massif were absent from this data set.

These comparisons with seismicity data from other OCCs on the MAR emphasize the unique nature of our observations. The diffuse, low-magnitude, high-rate (~300 events per day) seismicity that we observed at shallow depths beneath the Rainbow massif has not been observed at other OCCs, and the discrete fault structures observed at other OCCs were not observed at Rainbow. While some aspects of these differences could conceivably arise from differences in the seismic networks deployed at the various OCCs, it nevertheless seems clear that the seismogenic processes currently active at the Rainbow OCC are distinct from those observed at the TAG, Atlantis, Logatchev, and 13°20′N OCCs. The simplest explanation for this difference is that the detachment fault that exhumed the Rainbow massif is presently inactive, whereas detachment faulting was ongoing during seismicity surveys of the other OCCs. This raises the intriguing question as to what process(es) generated the diffuse, low-magnitude, shallow seismicity that we observed during our survey of the Rainbow massif.

4.3. Potential Seismogenic Mechanisms for the Rainbow Massif

The inability of our network to provide robust focal mechanism solutions for most of the observed seismicity limits our ability to constrain the nature of the source mechanism(s). Nevertheless, we may use the size, location, and rate of the observed activity to evaluate the plausibility of the various source mechanisms that might be expected in this geological setting, including tectonic extension/dissection of the massif, thermal strain, and hydrothermal alteration/serpentinization of the ultramafic massif.

Seismicity beneath the Rainbow massif exhibits a diffuse, dome-shaped pattern that roughly mimics the morphology of the massif itself (Figure 4). Projecting the hypocenters onto cross sections from the MCS profiles (Figure 10) shows that most are sandwiched in between the seafloor and subhorizontal reflectors in the MCS data, which have been interpreted to be magmatic sills intruded into ultramafic rock (Canales et al., 2017). In addition, the majority of events occurred in host rock with relatively fast *P* wave velocities indicative of ultramafic material with low to moderate degrees of serpentinization ($<$50%) or a mixture of mafic and ultramafic lithologies (Figure 11). This fast-velocity material is in many cases separated from the shallower, low-velocity material of the flanks by steeply dipping reflectors (Canales et al., 2017) that form an upper bound to the majority of hypocenters within the core of the massif (Figure 10). These observations lead to the conclusion that the seismicity primarily occurs in peridotite host rock that is being deformed by some combination of tectonic extension, thermal contraction, and serpentinization.

The conceptual model of McCaig et al. (2007) presents an idealized evolutionary model of an OCC in which hydrothermal activity is intimately related to activity along a detachment fault. In their model, slip along a

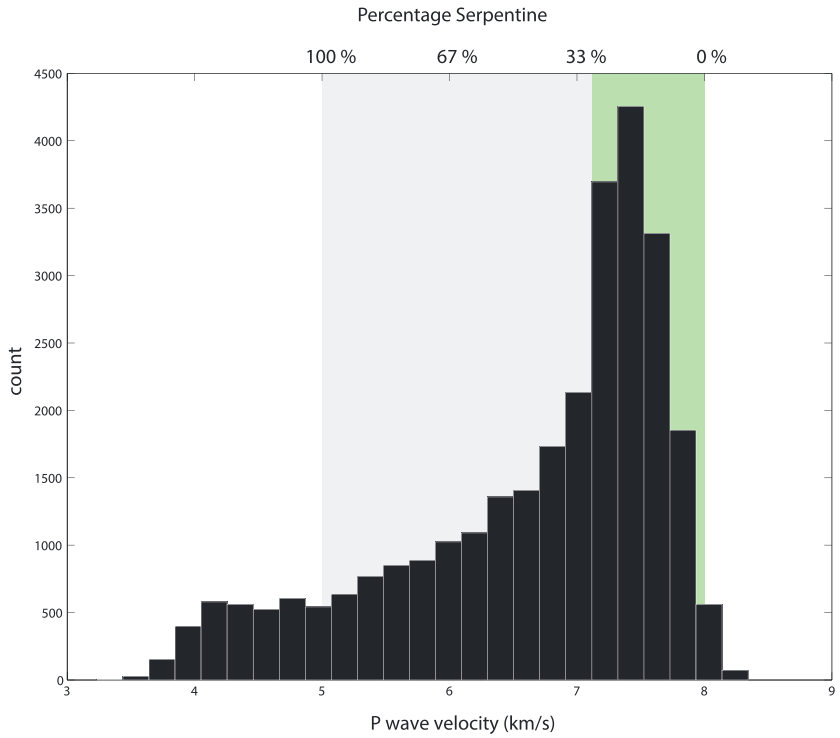

Figure 11. Histogram of *P* wave velocity in the 3-D velocity model of Dunn et al. (2017) at the hypocentral locations for events deeper than 500 m below the seafloor. Relationship between *P* wave velocity and degree of serpentinization of mantle peridotite shown on top axis. The green zone delimits the velocity range that uniquely corresponds to partially serpentinized peridotite. The gray region delimits the range where the correspondence between compressional velocity and lithology is equivocal and can be equally well explained by multiple rock types.

detachment provides a mechanism to channelize high-temperature hydrothermal fluids tapping heat from a partially molten zone at the ridge axis and/or within the detachment footwall. After the detachment becomes inactive, the McCaig et al. (2007) model predicts that hydrothermal activity should evolve from a high- to a low-temperature system like Lost City (Kelley et al., 2005). At the Rainbow massif we found no evidence for slip on an active detachment fault, supporting the assertion that the Rainbow detachment is presently inactive (Andreani et al., 2014), but the massif still hosts an energetic, high-temperature hydrothermal system. These observations indicate that the presence of an active detachment fault is not required to sustain high-temperature hydrothermal circulation within the massif, which is a departure from the McCaig et al. (2007) model, suggesting that other factors, such as the presence of melt bodies, control the nature of hydrothermal discharge at OCCs.

The volume of the seismically active region in our catalog is ~412 km^3, and with a total moment release of 3×10^{14} N m over 9 months and assuming a shear modulus of 71 GPa (Ben Ismail & Mainprice, 1998), we obtain a seismic strain rate (Ekstrom & England, 1989) of 8.9×10^{-9} yr^{-1}. If tectonic strain accommodates ~80% (Paulatto et al., 2015) of the full spreading rate of 21.5 mm/yr for this region (Le Douaran et al., 1982; Sloan & Patriat, 1992) across the ~10–15 km width of the massif/axial valley, then the tectonic strain rate would be on the order of $1–21 \times 10^{-6}$ yr^{-1}, which is several orders of magnitude higher than the seismic strain rate observed during our experiment. Tectonic processes thus provide more than enough strain to explain the moment release we observed, and the few reasonably well-constrained focal mechanism estimates that we obtained indicate oblique extension (Figure 9). In addition, there is a set of extensional faults that transect the massif (Andreani et al., 2014). Taken together, these observations suggest that tectonic extension of the massif is a plausible source mechanism for at least some of the observed seismicity. However, the high *b* value of 1.7 and the constant seismicity rates for our catalog are not consistent with tectonic source mechanisms, which typically have catalog *b* values of less than 1.5 and exhibit intermittent activity with mainshock-aftershock sequences (Frohlich & Davis, 1993; Gutenberg & Richter, 1955; Okal & Romanowicz, 1994). We therefore consider it unlikely that the microearthquakes were triggered by

tectonic processes, but we note that tectonic strain could have been released by events triggered by other processes.

Thermal strain is another potential source mechanism for the observed seismicity. Following Wilcock et al. (2002), the thermal strain rate for a volume of cooling crust is

$$\dot{\varepsilon}_{Hy} = \frac{Q\alpha_l}{V\rho c_p} \tag{1}$$

where Q is the heat flux, α_l is the coefficient of thermal expansion (5×10^{-5} K^{-1}; Liu & Lowell, 2009), ρ is the crustal density (2,700 kg/m^3; Hooft & Detrick, 1993), c_p is the specific heat capacity of the sills (1,400 J kg^{-1} K^{-1}; Liu & Lowell, 2009), and V is the volume of the cooling material. Most of the seismicity we observed was located in between subhorizontal reflectors imaged in the MCS data, interpreted to represent magmatic sills (Canales et al., 2017), and the seafloor. The MCS data do not constrain the melt fraction in the sills, and it is likely that many of these sills have already cooled completely, but the presence of high-temperature hydrothermal discharge on the massif indicates that at least one of the sills is hot enough to drive vigorous convection. When a magmatic sill cools, thermal strain develops within the sill as it contracts, which in turn leads to subsidence of the overlying material, forming graben-type structures with slip on steeply dipping faults above the sill margins (e.g., Bohnenstiehl & Carbotte, 2001). These types of grabens are not observed on or around the Rainbow massif, and well-defined, steeply dipping faults associated with graben formation are not observed in our seismicity data. This indicates that cooling of an individual magma sill to drive hydrothermal circulation is not a plausible mechanism for the observed seismicity. The distributed seismicity that we observed beneath the massif requires a more distributed form of cooling, which could arise if either (1) hydrothermal circulation is presently driven by cooling of a large number of magmatic sills or (2) the uplifted massif is conductively cooling en masse. The lack of active, high-temperature hydrothermal discharge at sites on the massif other than the main vent argues against the first scenario, but the uplifted mantle material in the massif is conductively cooling with a heat flux estimated to be ~0.03 GW (Canales et al., 2017). Assuming that the volume of cooling material is equal to the volume of the seismogenic zone (~412 km^3), we obtain a thermal strain rate estimate for conductive cooling (3×10^{-8} yr^{-1}) that is an order of magnitude greater than our observed seismic strain rate. Conductive cooling of the massif would lead to distributed deformation within the massif, which is broadly consistent with the observed hypocentral patterns. These considerations suggest that widespread subsolidus cooling and contraction of uplifted mantle material is a plausible mechanism for at least some of the observed seismicity.

It is clear from the composition of the hydrothermal fluids being discharged at the RHF (Charlou et al., 2002) and the rock samples acquired from the massif (Andreani et al., 2014) that the ultramafic massif is being actively serpentinized by hydrothermal circulation. The location of the microearthquake hypocenters in largely ultramafic rocks (Figure 11) above the magmatic sills (Figure 10) driving hydrothermal convection suggests that serpentinite alteration may play a role in generating the observed seismicity. Serpentinization of peridotite increases the solid volume of the rock (O'Hanley, 1992), which can generate fractures either at the microscale due to intragrain stresses (Kelemen & Hirth, 2012) or at the regional scale due to buoyant diapirism within the massif (Bonatti, 1976). If the observed seismicity was generated by volume change in the host rock from serpentinization, then we can use the relationship of Mcgarr (1976) to relate the volume change to the moment release,

$$\sum M_o = K\mu|\Delta V| \tag{2}$$

where $K = 1$ for a pure volume increase crack opening in one direction, μ is the modulus of rigidity (71 GPa), and ΔV is the total volume change associated with the event catalog. Using this equation, we obtain a total volume change of 4×10^{-6} km^3 associated with our catalog, which is small compared to the total serpentine volume of ~280 km^3 within the massif inferred from seismic velocity data (Canales et al., 2017). These estimates must be treated with caution, however, because the applicability of equation (2) for the serpentinization process has not been validated, and it is possible that some, up to and including all, of the volume strain from serpentinization could be released aseismically.

The results from our application of the collapsing method (Jones & Stewart, 1997) to the hypocentral catalog indicate that a significant fraction of the seismicity may have originated from within a relatively narrow depth

interval at ~3 km below the seafloor (Figure 4), which is notable because serpentinization rates are strongly temperature dependent, with maximum rates occurring at temperatures between 250 and 320°C (McCollom et al., 2016). Kinetic limitations (i.e., dissolution and precipitation) reduce reaction rates at temperatures below this range, and olivine is completely stable in the presence of water at temperatures greater than ~400°C (Lamadrid et al., 2017; McCollom et al., 2016). Thus, if the microearthquakes were generated by serpentinization, we would expect a high density of events in a relatively narrow depth zone bounded by the ~250–320°C isotherms, and in our results we see such a band at a depth of ~3 km below the seafloor. Based on the depth uncertainty of the hypocentral catalog, this band could plausibly be as shallow as 2 km, and as deep as 4 km, below the seafloor.

The space-time character of the microearthquake hypocenters require a source process that has a steady rate over the 9 month interval of our deployment and that is distributed over essentially the entire area of the massif. These characteristics are consistent with a serpentinization source mechanism, since seawater is presumably altering the massif en masse, which would also uplift the massif via buoyant diapirism (Bonatti, 1976) due to the volume increase from serpentinization (e.g., Coleman, 1971). This mechanism has been invoked to explain the uplift of other OCCs, such as TAG (Germanovich et al., 2012) and Atlantis massif (Blackman et al., 2008; Karson et al., 2006), and could contribute to present-day uplift and deformation of the Rainbow massif.

The microearthquake hypocenters at Rainbow evolve from a diffuse cloud of activity deeper in the massif into a more focused, ring-like pattern in the shallow crust (Figure 5). Interestingly, this ring structure underlies the known sites of active and fossil hydrothermal discharge on the massif, suggesting that this shallow activity may be related to hydrothermal flow. If high-temperature fluids in the shallow crust are restricted to narrow hydrothermal upflow zones, then serpentinization of the shallow crust will be focused in these zones, and this might explain the ring-like structure of seismicity we observe at shallow depths.

Based on these considerations, we conclude that serpentinization is a plausible source mechanism for the seismicity observed beneath the Rainbow massif. However, a direct link between serpentinization and seismic activity has not been established in either laboratory or field studies. Although serpentinization has been directly linked to fracture generation in laboratory experiments (Plümper et al., 2012) and outcrops (Kelemen & Hirth, 2012), whether or not this fracturing is associated with detectable seismicity remains an open question. Thus, while we know that the massif is actively being serpentinized, and that the massif generates a unique type of high-rate, low-magnitude seismicity, we lack a theoretical or empirical basis for directly linking these two observations. This issue could be addressed in the future by (1) laboratory serpentinization experiments that include instrumentation to detect acoustic emissions and (2) deployment of microearthquake networks in actively serpentinizing regions that are capable of resolving nondouble-couple, volume change focal mechanisms.

To summarize our source mechanism analysis, the seismicity we observed beneath the Rainbow massif is unlike any other microearthquake data set acquired from a MOR setting to date in that it represents high-rate, diffuse deformation of shallow, ultramafic rocks. A subset of these events appears to be associated with mass wasting on the northwest flank of the massif, but the evidence constraining the mechanism driving the majority of the seismicity is equivocal. Tectonic extension, thermal contraction, and serpentine alteration are presumably all active processes at the Rainbow massif, and they all likely generate higher strain rates than those estimated from the seismic moment release we observed. However, the space-time characteristics and the magnitude distribution of our hypocentral catalog are most consistent with a thermal or alteration source mechanism that generates small earthquakes at essentially constant rates across the entire uplifted massif. In addition, most of the seismicity occurred in regions where seismic refraction data indicate the presence of ultramafic rocks, and the collapsing method results suggest that a high density of events may have occurred within a narrow depth band, consistent with thermal controls on the serpentinization reaction. These aspects of the hypocentral patterns are strongly suggestive of a serpentinization source mechanism, and hydrothermal fluids sampled at the Rainbow massif demonstrate that serpentinization is an active process within the massif. Taken together, the body of evidence points toward serpentinization as a likely source mechanism for the seismicity we observed, but this interpretation is necessarily equivocal in light of the fact that we could not constrain the focal mechanisms for the vast majority of the microearthquakes.

5. Conclusions

From our analysis of microearthquake data acquired from the Rainbow massif we conclude that

1. Low-magnitude earthquakes at the Rainbow massif occur at an essentially constant rate with no swarm-like behavior and no mainshock-aftershock sequences. The events are distributed in a region sandwiched in between magmatic sills imaged by MCS reflections and the seafloor, with no spatial patterns related to a fault surface, indicating that the detachment fault responsible for the exhumation of the massif is likely no longer active, consistent with seafloor geological observations. This a fundamental difference between the seismicity of Rainbow and that observed at other MAR OCCs such as TAG, Atlantis massif, Logatchev, and 13°20′N.
2. A subset of shallow events on the northwest flank of the massif is correlated with a prominent reflector in the MCS data and is interpreted to represent mass wasting via low-angle sliding of a coherent block of ultramafic material.
3. The observed seismicity was generated by some combination of tectonic extensional strain, volumetric strain from serpentinization of the massif, and thermal strain from cooling of the uplifted massif. These mechanisms are not mutually exclusive, and it seems likely that all of these processes contributed in some way to the observed seismicity. However, the space-time and magnitude characteristics of the hypocentral catalog, along with contextual geological data, are most consistent with widespread serpentinization of the ultramafic massif.
4. The lack of seismicity associated with an active detachment fault argues against models in which active detachments are needed to focus and sustain high-temperature hydrothermal activity within the footwall of OCCs. Instead, our results, combined with seismic imaging results, indicate that high-temperature hydrothermal discharge is driven by magmatic intrusions, even when a detachment fault is inactive.

Acknowledgments

We are grateful to the captains, crews, technical staff, and scientific party during both cruises (R/V *Marcus G. Langseth* cruise MGL1305 and R/V *Pelagia* cruise 64PE382), for their valuable assistance in collecting the data. We thank the OBSIP Management Office and the personnel of the SIO and WHOI Institutional Instrument Contributors for their technical support during OBS operations. We are grateful to J. Sileny, Z. Jechumtalova, and V. Vavrycuk for assistance with our focal mechanism analyses. This research was supported by NSF grants OCE-0961680 to J. P. C. and R. S. and OCE-0961151 to R. D. Data used in this research were provided by instruments from the Ocean Bottom Seismograph Instrument Pool (http://www.obsip.org) which is funded by the National Science Foundation. OBSIP data are archived at the IRIS Data Management Center (http://www.iris.edu) under code X3 (http://doi.org/10.7914/SN/X3_2013). The hypocenter catalog for all locatable events is available from the IEDA repository (http://dx.doi.org/10.1594/IEDA/324328). The manuscript was significantly improved by constructive reviews from Ingo Grevemeyer, Martin Scherwath, and Associate Editors Cliff Frolich and Gail Christeson.

References

Andreani, M., Escartin, J., Delacour, A., Ildefonse, B., Godard, M., Dyment, J., … Fouquet, Y. (2014). Tectonic structure, lithology, and hydrothermal signature of the Rainbow massif (Mid-Atlantic Ridge 36°14′N). *Geochemistry, Geophysics, Geosystems*, *15*, 3543–3571. https://doi.org/10.1002/2014GC005269

Ben Ismail, W., & Mainprice, D. (1998). An olivine fabric database: An overview of upper mantle fabrics and seismic anisotropy. *Tectonophysics*, *296*(1-2), 145–157. https://doi.org/10.1016/S0040-1951(98)00141-3

Blackman, D. K., Ildefonso, B., John, B. E., Ohara, Y., Miller, D. J., Abe, N., … Zhao, X. (2011). Drilling constraints on lithospheric accretion and evolution at Atlantis massif, Mid-Atlantic Ridge 30°N. *Journal of Geophysical Research*, *116*, B07103. https://doi.org/10.1029/2010JB007931

Blackman, D. K., Karner, G., & Searle, R. C. (2008). Three-dimensional structure of oceanic core complexes: Effects on gravity structure and ridge flank morphology, Mid-Atlantic Ridge 30°N. *Geochemistry, Geophysics, Geosystems*, *6*, Q06007. https://doi.org/10.01029/02008GC001951

Bohnenstiehl, D. R., & Carbotte, S. M. (2001). Faulting patterns near 19°30′S on the East Pacific Rise: Fault formation and growth at a superfast spreading center. *Geochemistry, Geophysics, Geosystems*, *2*, 1056. https://doi.org/10.1029/2001GC000156.

Bonatti, E. (1976). Serpentinite protrusions in the oceanic crust. *Earth and Planetary Science Letters*, *32*(2), 107–113. https://doi.org/10.1016/0012-821X(76)90048-0

Brune, J. N. (1970). Tectonic stress and spectra of seismic shear waves from earthquakes. *Journal of Geophysical Research*, *75*(26), 4997–5009. https://doi.org/10.1029/JB075i026p04997

Canales, J. P., Dunn, R. A., Arai, R., & Sohn, R. A. (2017). Seismic imaging of magma sills beneath an ultramafic-hosted hydrothermal system. *Geology*, *45*(5), 451–454. https://doi.org/10.1130/G38795.1

Canales, J. P., Dunn, R. A., Swift, S., Paulatto, M., Arai, R., Szitkar, F., … Sohn, R. A. (2013). MARINER: Seismic investigation of the Rainbow hydrothermal field and its tectono/magmatic setting, Mid-Atlantic Ridge 36 14′N—A report from RV *M.G. Langseth* cruise MGL1305. *Inter Ridge News*, *22*, 43–50.

Cann, J. R., & Strens, M. R. (1982). Black smokers fuelled by freezing magma. *Nature*, *298*(5870), 147–149. https://doi.org/10.1038/298147a0

Cannat, M. (1993). Emplacement of mantle rocks in the seafloor at mid-ocean ridges. *Journal of Geophysical Research*, *98*(B3), 4163–4172. https://doi.org/10.1029/92JB02221

Cannat, M., Mangeney, A., Ondréas, H., Fouquet, Y., & Normand, A. (2013). High-resolution bathymetry reveals contrasting landslide activity shaping the walls of the Mid-Atlantic Ridge axial valley. *Geochemistry, Geophysics, Geosystems*, *14*, 1524–2027. https://doi.org/10.1002/ggge.20056

Cannat, M., Mevel, C., Maia, M., Deplus, C., Durand, C., Gente, P., … Reynolds, J. (1995). Thin crust, ultramafic exposures, and rugged faulting patterns at the Mid-Atlantic Ridge (22°–24°N). *Geology*, *23*(1), 49–52. https://doi.org/10.1130/0091-7613(1995)023%3C0049:TCUEAR%3E2.3.CO;2

Charlou, J. L., Donval, J. P., Fouquet, Y., Jean-Baptiste, P., & Holm, N. (2002). Geochemistry of high H_2 and CH_4 vent fluids issuing from ultramafic rocks at the Rainbow hydrothermal field (36°14′N, MAR). *Chemical Geology*, *191*(4), 345–359. https://doi.org/10.1016/S0009-2541(02)00134-1

Christensen, N. I. (2004). Serpentinites, peridotites, and seismology. *International Geology Review*, *46*(9), 795–816. https://doi.org/10.2747/0020-6814.46.9.795

Coleman, R. G. (1971). Petrological and geophysical nature of serpentinites. *Geological Society of America Bulletin*, *82*(4), 897–918. https://doi.org/10.1130/0016-7606(1971)82%5B897:PAGNOS%5D2.0.CO;2

Collins, J. A., Smith, D. K., & McGuire, J. J. (2012). Seismicity of the Atlantis massif detachment fault, 30°N at the Mid-Atlantic Ridge. *Geochemistry, Geophysics, Geosystems*, *13*, Q0AG11. https://doi.org/10.1029/2012GC004210

Deichmann, N. (2006). Local magnitude, a moment revisited. *Bulletin of Seismological Society of America*, *96*(4A), 1267–1277. https://doi.org/10.1785/0120050115

Deichmann, N. (2017). Theoretical basis for the observed break in M_L/M_W scaling between small and large earthquakes. *Bulletin of Seismological Society of America*, *107*(2), 505–520. https://doi.org/10.1785/0120160318

deMartin, B. J., Reves-Sohn, R., Canales, J. P., & Humphris, S. E. (2007). Kinematics and geometry of active detachment faulting beneath the Trans-Atlantic Geotraverse (TAG) hydrothermal field on the Mid-Atlantic Ridge. *Geology*, *35*(8), 711–714. https://doi.org/10.1130/G23718A.1

Douville, E., Charlou, J. J., Oelkers, E. H., Bienvenu, P., Jove Colon, C. F., Donval, J. P., … Appriou, P. (2002). The Rainbow vent fluids (36°14′N, MAR): The influence of ultramafic rocks and phase separation on trace metal content in Mid-Atlantic Ridge hydrothermal fluids. *Chemical Geology*, *184*(1-2), 37–48. https://doi.org/10.1016/S0009-2541(01)00351-5

Dunn, R. A., Arai, R., Eason, D. E., Canales, J. P., & Sohn, R. A. (2017). Three-dimensional seismic structure of the mid-Atlantic ridge: An investigation of tectonic, magmatic, and hydrothermal processes in the rainbow area. *Journal of Geophysical Research: Solid Earth*, *122*, 9580–9602. https://doi.org/10.1002/2017JB015051

Dziewonski, A. M., Chou, T. A., & Woodhouse, J. H. (1981). Determination of earthquake source parameters from waveform data for studies of global and regional seismicity. *Journal of Geophysical Research*, *86*(B4), 2825–2852. https://doi.org/10.1029/JB086iB04p02825

Eason, D. E., Dunn, R. A., Pablo Canales, J., & Sohn, R. A. (2016). Segment-scale variations in seafloor volcanic and tectonic processes from multibeam sonar imaging, Mid-Atlantic Ridge Rainbow region (35°45′–36°35′N). *Geochemistry, Geophysics, Geosystems*, *17*, 3560–3579. https://doi.org/10.1002/2016GC006433

Ekstrom, G., & England, P. (1989). Seismic strain rates in regions of distributed continental deformation. *Journal of Geophysical Research*, *94*(B8), 10,231–10,257. https://doi.org/10.1029/JB094iB08p10231

Ekstrom, G., Nettles, M., & Dziewonski, A. M. (2012). The global CMT project 2004–2010: Centroid-moment tensors for 13,017 earthquakes. *Physics of the Earth and Planetary Interiors*, *200*, 1–9.

Fouquet, Y., Barriga, F., Charlou, J. L., Elderfield, H., German, C. R., Ondreas, H., … Stephan, M. (1998). FLORES diving cruise with the Nautile near the Azores—First dives on the Rainbow field: Hydrothermal seawater/mantle interaction. *InterRidge News*, *7*(1), 24–28.

Frohlich, C., & Davis, S. D. (1993). Teleseismic *b*-values—Or, much ado about 1.0. *Journal of Geophysical Research*, *98*(B1), 631–644. https://doi.org/10.1029/92JB01891

German, C. R., & Parson, L. M. (1998). Distributions of hydrothermal activity along the Mid-Atlantic Ridge: Interplay of magmatic and tectonic controls. *Earth and Planetary Science Letters*, *160*(3-4), 327–341. https://doi.org/10.1016/S0012-821X(98)00093-4

German, C. R., Parson, L. M., & Team, H. S. (1996). Hydrothermal exploration near the Azores Triple Junction: Tectonic control of venting at slow-spreading ridges. *Earth and Planetary Science Letters*, *138*(1-4), 93–104. https://doi.org/10.1016/0012-821X(95)00224-Z

German, C. R., Thurnherr, A. M., Knoery, J., Charlou, J. L., Jean-Baptiste, P., & Edmonds, H. N. (2010). Heat, volume and chemical fluxes from submarine venting: A synthesis of results from the Rainbow hydrothermal field, 36°N MAR. *Deep-Sea Research Part I*, *57*(4), 518–527. https://doi.org/10.1016/j.dsr.2009.12.011

Germanovich, L. N., Genc, G., Lowell, R. P., & Rona, P. A. (2012). Deformation and surface uplift associated with serpentinization at mid-ocean ridges and subduction zones. *Journal of Geophysical Research*, *117*, B07103. https://doi.org/10.1029/2012JB009372

Gràcia, E., Charlou, J.-L., Radford-Knoery, J., & Parson, L. M. (2000). Non-transform offsets along the Mid-Atlantic Ridge south of the Azores (38°N–34°N): Ultramafic exposures and hosting of hydrothermal vents. *Earth and Planetary Science Letters*, *177*(1-2), 89–103. https://doi.org/10.1016/S0012-821X(00)00034-0

Grevemeyer, I., Reston, T. J., & Moeller, S. (2013). Microseismicity of the Mid-Atlantic Ridge at 7°S–8°15′S and at the Logatchev massif oceanic core complex at 14°40′N–14°50′N. *Geochemistry, Geophysics, Geosystems*, *14*, 3532–3554. https://doi.org/10.1002/ggge.20197

Grindlay, N. R., & Fox, P. J. (1993). Lithospheric stresses associated with nontransform offsets of the Mid-Atlantic Ridge—Implications from a finite-element analysis. *Tectonics*, *12*(4), 982–1003. https://doi.org/10.1029/93TC00364

Gutenberg, B., & Richter, C. F. (1955). Magnitude and energy of earthquakes. *Nature*, *176*(4486), 795–795. https://doi.org/10.1038/176795a0

Hanks, T. C., & Thatcher, W. (1972). A graphical representation of seismic source parameters. *Journal of Geophysical Research*, *77*(23), 4393–4405. https://doi.org/10.1029/JB077i023p04393

Hardebeck, J. L., & Shearer, P. M. (2002). A new method for determining first-motion focal mechanisms. *Bulletin of the Seismological Society of America*, *92*(6), 2264–2276. https://doi.org/10.1785/0120010200

Hardebeck, J. L., & Shearer, P. M. (2003). Using *S*/*P* amplitude ratios to constrain the focal mechanisms of small earthquakes. *Bulletin of the Seismological Society of America*, *93*(6), 2434–2444. https://doi.org/10.1785/0120020236

Harding, A. J., Arnulf, A. F., & Blackman, D. K. (2016). Velocity structure near IODP Hole U1309D, Atlantis massif, from waveform inversion of streamer data and borehole measurements. *Geochemistry, Geophysics, Geosystems*, *17*, 1990–2014. https://doi.org/10.1002/2016GC006312

Hooft, E., & Detrick, R. S. (1993). The role of density in the accumulation of basaltic melts at mid-ocean ridges. *Geophysical Research Letters*, *20*(6), 423–426. https://doi.org/10.1029/93GL00295

Jones, R. H., & Stewart, R. C. (1997). A method for determining significant structures in a cloud of earthquakes. *Journal of Geophysical Research*, *102*(B4), 8245–8254. https://doi.org/10.1029/96JB03739

Karson, J. A., Früh-Green, G. L., Kelley, D. S., Williams, E. A., Yoerger, D. R., & Jakuba, M. (2006). Detachment shear zone of the Atlantis massif core complex, Mid-Atlantic Ridge, 30°N. *Geochemistry, Geophysics, Geosystems*, *7*, Q06016. https://doi.org/10.01029/02005GC001109

Kelemen, P. B., & Hirth, G. (2012). Reaction-driven cracking during retrograde metamorphism: Olivine hydration and carbonation. *Earth and Planetary Science Letters*, *345*, 81–89.

Kelley, D. S., Karson, J. A., Früh-Green, G. L., Yoerger, D., Shank, T. M., Butterfield, D. A., … Sylva, S. P. (2005). A serpentinite-hosted ecosystem: The Lost City hydrothermal field. *Science*, *307*(5714), 1428–1434. https://doi.org/10.1126/science.1102556

Kelley, D. S., & Shank, T. M. (2013). A decade of discovery in slow spreading environments. In *Diversity of hydrothermal systems on slow spreading ocean ridges* (pp. 369–407). Washington, DC: American Geophysical Union.

Lamadrid, H. M., Rimstidt, J. D., Schwarzenbach, E. M., Klein, F., Ulrich, S., Dolocan, A., & Bodnar, R. J. (2017). Effect of water activity on rates of serpentinization of olivine. *Nature Communications*, *8*, 16,107. https://doi.org/10.1038/ncomms16107

Lartaud, F., de Rafaelis, M., Oliver, G., Krylova, E., Dyment, J., Ildefonse, B., … Le Bris, N. (2010). Fossil clams from a serpentinite-hosted sedimented vent field near the active smoker complex Rainbow, MAR, 36°13′N: Insight into the biogeography of vent fauna. *Geochemistry, Geophysics, Geosystems*, *11*, Q0AE01. https://doi.org/10.1029/2010GC003079

Lartaud, F., Little, C. T. S., de Rafaelis, M., Bayon, G., Dyment, J., Ildefonse, B., … Le Bris, N. (2011). Fossil evidence for serpentinization fluids fueling chemosynthetic assemblages. *Proceedings of the National Academy of Sciences of the United States of America*, *108*(19), 7698–7703. https://doi.org/10.1073/pnas.1009383108

Le Douaran, S., Needham, H. D., & Francheteau, J. (1982). Pattern of opening rates along the axis of the Mid-Atlantic Ridge. *Nature*, *300*(5889), 254–257. https://doi.org/10.1038/300254a0

Lee, W. H. K., & Stewart, S. W. (1981). *Principles and applications of microearthquake networks*. San Diego, CA: Academic.

Liu, L., & Lowell, R. P. (2009). Models of hydrothermal heat output from a convecting, crystallizing, replenished magma chamber beneath an oceanic spreading center. *Journal of Geophysical Research*, *114*, B02102. https://doi.org/10.01029/02008JB005846

McCaig, A. M., Cliff, R. A., Escartín, J., Fallick, A. E., & MacLeod, C. J. (2007). Oceanic detachment faults focus very large volumes of black smoker fluids. *Geology*, *35*(10), 935–938. https://doi.org/10.1130/G23657A.1

McCollom, T. M., Klein, F., Robbins, M., Moskowitz, B., Berquo, T. S., Jons, N., … Templeton, A. (2016). Temperature trends for reaction rates, hydrogen generation, and partitioning of iron during experimental serpentinization of olivine. *Geochimica et Cosmochimica Acta*, *181*, 175–200. https://doi.org/10.1016/j.gca.2016.03.002

Mcgarr, A. (1976). Seismic moments and volume changes. *Journal of Geophysical Research*, *81*(8), 1487–1494. https://doi.org/10.1029/JB081i008p01487

Menke, W. (2005). In A. Levander & G. Nolet (Eds.), *Case studies of seismic tomography and earthquake location in a regional context, in seismic Earth: Array analysis of broadband seismograms*. Washington, DC: American Geophysical Union.

Miller, D. J., & Christensen, N. I. (1997). Seismic velocities of lower crustal and upper mantle rocks from the slow spreading Mid-Atlantic Ridge, south of the Kane transform zone (MARK). *Proceedings of the Ocean Drilling Program - Scientific Results*, *153*, 437–454.

O'Hanley, D. S. (1992). Solution to the volume problem in serpentinization. *Geology*, *20*(8), 705–708. https://doi.org/10.1130/0091-7613(1992)020%3C0705:STTVPI%3E2.3.CO;2

Okal, E. A., & Romanowicz, B. A. (1994). On the variation of *b*-values with earthquake size. *Physics of the Earth and Planetary Interiors*, *87*(1-2), 55–76. https://doi.org/10.1016/0031-9201(94)90021-3

Parnell-Turner, R., Sohn, R. A., Pierce, C., Reston, T. J., MacLeod, C. J., Searle, R. C., & Simao, N. M. (2017). Oceanic detachment faults generate compression in extension. *Geology*, *45*(10), 923–926. https://doi.org/10.1130/G39232.1

Parson, L., Gràcia, E., Coller, D., German, C., & Needham, D. (2000). Second order segmentation; the relationship between volcanism and tectonism at the MAR, 38°–35°40′N. *Earth and Planetary Science Letters*, *178*(3-4), 231–251. https://doi.org/10.1016/S0012-821X(00)00090-X

Paulatto, M., Canales, J. P., Dunn, R. A., & Sohn, R. A. (2015). Heterogeneous and asymmetric crustal accretion: New constraints from multi-beam bathymetry and potential field data from the Rainbow area of the Mid-Atlantic Ridge (36°15′N). *Geochemistry, Geophysics, Geosystems*, *16*, 2994–3014. https://doi.org/10.1002/2015GC005743

Plümper, O., Røyne, A., Magrasó, A., & Jamtveit, B. (2012). The interface-scale mechanism of reaction-induced fracturing during serpentinization. *Geology*, *40*(12), 1103–1106. https://doi.org/10.1130/g33390.1

Scholz, C. H. (1968). The frequency-magnitude relation of microfracturing in rock and its relation to earthquakes. *Bulletin of Seismological Society of America*, *58*(1), 399–415.

Sileny, J., Jechumtalova, Z., & Dorbath, C. (2014). Small scale earthquake mechanisms induced by fluid injection at the enhanced geothermal system reservoir Soultz (Alsace) in 2003 using alternative source models. *Pure and Applied Geophysics*, *171*(10), 2783–2804. https://doi.org/10.1007/s00024-013-0750-2

Simao, N., Escartín, J., Goslin, J., Haxel, J., Cannat, M., & Dziak, R. P. (2010). Regional seismicity of the Mid-Atlantic Ridge: Observations from autonomous hydrophone arrays. *Geophysical Journal International*, *183*(3), 1559–1578. https://doi.org/10.1111/j.1365-246X.2010.04815.x

Sloan, H., & Patriat, P. (1992). Kinematics of the North American-African plate boundary between 28° and 29° during the last 10 Ma: Evolution of the axial geometry and spreading rate and direction. *Earth and Planetary Science Letters*, *113*(3), 323–341. https://doi.org/10.1016/0012-821X(92)90137-K

Sohn, R., Canales, J., & Dunn, R. (2018). Hypocenter catalog data from the Mid-Atlantic Ridge—Rainbow Vent Field acquired in 2013. *Integrated Earth Data Applications (IEDA)*. https://doi.org/10.1594/IEDA/324328

Spencer, S., Smith, D. K., Cann, J. R., Lin, J., & McAllister, E. (1997). Structure and stability of non-transform discontinuities on the Mid-Atlantic Ridge between 24° and 30°N. *Marine Geophysical Researches*, *19*(4), 339–362. https://doi.org/10.1023/A:1004200411959

Thurnherr, A. M., & Richards, K. J. (2001). Hydrography and high-temperature heat flux of the Rainbow hydrothermal site (36°14′N, Mid-Atlantic Ridge). *Journal of Geophysical Research*, *106*(C5), 9411–9426. https://doi.org/10.1029/2000JC900164

Waldhauser, F., & Ellsworth, W. L. (2000). A double-difference earthquake location algorithm: Method and application to the northern Hayward fault. *Bulletin of Seismological Society of America*, *90*(6), 1353–1368. https://doi.org/10.1785/0120000006

Wilcock, W. S. D., Archer, S. D., & Purdy, G. M. (2002). Microearthquakes on the Endeavour segment of the Juan de Fuca Ridge. *Journal of Geophysical Research*, *107*(B12), 2336. https://doi.org/10.1029/2001JB000505